Word count: 7138 **Revision 2**

Improving grain size analysis using computer vision techniques and implications for grain growth kinetics

Isra S. Ezad[1*], Joshua F. Einsle[2], David P. Dobson[1], Simon A. Hunt[3], Andrew R, Thomson[1], John P. Brodholt[1]

[1]Department of Earth Sciences, UCL, Gower Street, London, WC1E 6BT

[2]School of Geographical and Earth Sciences, University of Glasgow, Glasgow, G12 8QQ

[3]Department of Materials, University of Manchester, Sackville Street Building, Manchester, M1 3BB

Abstract

Earth's physical properties and mantle dynamics are strongly dependent on mantle grain size, shape and orientation, these characteristics are however poorly constrained. Experimental studies provide an opportunity to simulate the grain growth kinetics of mantle aggregates. The experimentally determined grain sizes can be fit to the normal grain growth law ($G^n - G_0^n) = k_0 t. exp\left(\frac{-\Delta H}{RT}\right)$ and then be used to determine grain size throughout the mantle and geological time. The grain growth dynamics of spinel – orthopyroxene mixtures in the upper mantle are modelled here, by experimentally producing small grain sizes in the range of 0.5 to 2 μm radius at pressures and temperatures equivalent to the spinel lherzolite stability field. To accurately measure the sizes of these small grains we have developed a computer vision

* Present address: Department of Earth and Environmental Sciences, Macquarie University, Balaclava Road, Sydney, 2109

workflow; using a watershed transformation which rapidly measures 68% more grains and produces a 20% improvement in the average grain size accuracy and repeatability when compared with manual methods. Using this automated approach, we have been able to identify a significant proportion of small grains which have been overlooked when using manual methods. This additional population of grains, when fit to the normal grain growth law, highlights the influence of improved accuracy and sample size on the estimation of grain growth kinetic parameters. Our results demonstrate that automatic computer vision enables a systematic, fast, repeatable method of grain size analysis, across large data sets, improving the accuracy of experimentally determined grain growth kinetics.

Introduction

Rocks are composed of large numbers of grains, or crystallites. A grain is formed of a coherent continuous lattice, the boundary of which has a discontinuous change in crystal lattice or other properties. The properties of these grains: their size, shape, orientation and how they interact, influence the bulk properties of rocks. These aggregate properties influence many of Earth's physical properties including strength or viscosity, and seismic anisotropy; these in turn impact the large scale motion of plates and mantle overturns (Bercovici and Ricard 2013; Chu and Korenaga 2012; Dannberg et al. 2017; Evans et al. 2001; Hirth and Kohlstedt 1995; Karato 1984; Yamazaki et al. 2010). On a smaller length scale, grain size is often used as the basis for the classification of some igneous and clastic rocks, as well as interpretations of the geological environment and the processes which formed it. Grain growth and recrystallisation are active processes, continuously changing the grain size of mantle aggregates. This has far reaching consequences, for example, the decoupling of the upper and lower mantle may be due to a sudden grain size reduction associated with the spinel to perovskite transformation at the 660 km discontinuity (Dobson and Mariani 2014).

Interpreting indirect geophysical observations in terms of grain-size is extremely difficult and therefore the aggregate grain-size of the mantle is poorly constrained. It is widely thought to vary from millimeters to centimeters at ~400 km depth, close to the transition zone (Faul and Jackson, 2005). Estimates of the lower mantle (depths > 660km) grain-size may vary from 1 to 1000 μm (Solomatov et al. 2002; Solomatov and Reese 2008). Constraining the evolution of grain size of the mantle by experiments is difficult because they are limited by both extent, sample volume and result in small grain sizes tens of micrometers at most (Karato 1989; Kim et al. 2004; Faul and Jackson 2005; Yamazaki et al. 2005, 2010; Faul and Scott 2006; Nishihara et al. 2006; Hiraga et al. 2010b). The experimental pressure—temperature—time series results are extrapolated over many orders of magnitude to mantle scales using kinetic models (Hillert 1965; Chu and Korenaga 2012). These models assume the normal grain growth law:

$$G^n - G_0^n = kt, \quad (1)$$

where G is grain size, G_0 the initial grain size, k rate constant, t time and n the grain growth exponent. The rate constant, k, has an Arrhenius temperature dependence and a global fit can be applied of the form:

$$(G^n - G_0^n) = k_0 t.exp\left(\frac{-\Delta H}{RT}\right), \quad (2)$$

where k_0 is the pre-exponential exponent, H the activation enthalpy for grain growth and R is the gas constant.

Accurate simulation of grain growth under realistic mantle conditions and time frames requires a very well constrained grain growth exponent (n). Determination of the grain growth exponent for any set of experiments relies on accurate measurement of the grain size, reproduced through annealing experiments. This requires imaging and analyzing of statistically significant numbers of grains, often thousands, across multiple experiments. Ideally, the grain measurements produce 2D log-normal distributions, which can describe

70 normal grain growth occurring in 3D space (Hillert 1965; Saetre 2002; Rios and Zöllner
71 2018) and kinetic grain growth parameters (Burke and Turnbull 1952).

72 We examine a two-phase system spinel and orthopyroxene as an analogue to the
73 composition of the upper mantle. In grain growth experiments this two-phase system splits
74 into two compositionally distinct phases and grains ranging in size from roughly 0.5 μm to 2
75 μm. These properties of the two phase system indicated that the most effective method for
76 measuring large volumes of grains from multiple samples is, back scatter electron, scanning
77 electron microscopy (BSE-SEM). This microscopic technique provides high spatial
78 resolution, with a contrast mechanism largely dominated by the average atomic mass of the
79 material examined. The experimental samples then image as bright spinel grains against a
80 dark largely uniform background of orthopyroxene. This high contrast system provides an
81 excellent test bed for developing automated techniques for detecting and measuring grains,
82 especially when the greater number of grains measured directly translates to an improved
83 ability to estimate kinetic parameters.

84 Manual measurement techniques such as the "intercept" (Mendelson 1969; Abrams
85 1971) and/or "areas of equivalent circles" methods still comprise a major technique for the
86 study of grain size. We focus on this comparison since a recent literature search shows the
87 “areas of equivalent circles” has been referenced 779[1] times in peer-reviewed scientific
88 articles within the last six years, whilst the “intercept method” has been referenced 602[2]
89 times. Furthermore, the common use of manual measurement for industrial applications is
90 highlighted by the published standard by ASTM International for the intercept method
91 (ASTM E112-13 2012). This standard highlights the central problem with manual methods,

[1] Number of articles was found using Scopus search, key words of "area of equivalent circles" and "grain size" were used in a search period between 2014-2020

[2] Number of articles was found using Scopus search, key words of "intercept" and "grain size" were used in a search period between 2014-2020

low throughput of 15 minutes per image for an expert analysist, and a large ±16% uncertainty in measured grain sizes. For this study, manual grain size analysis of 30 sample images required over 7.5 hours of expert level analysis time. Moreover, these analysis methods are more difficult for complex samples with clustered grains or samples with complex grain shapes. There is therefore a clear need for automated image processing as an alternative, faster, independent method of analysis for grain size estimation from images.

As noted above the study here leverages the high contrast between spinel and orthopyroxene with BSE-SEM microscopy to acquire sufficient 2D images for a log-normal sample distribution. The computer vision methods developed here are general enough that they can be applied and adapted to a wide range of other microscopic modalities, especially since virtually all images collected these days are digital. Segmenting optical images follows largely the same process as will be demonstrated below for BSE-SEM images. Likewise, the challenges of segmenting three-dimensional X-Ray tomography data can be viewed as a generalization of the methods presented here. Finally, microanalytical techniques such as energy dispersive x-ray spectroscopy (EDS) or electron backscatter diffraction (EBSD) offer methods for not only identifying grains but examining compositional or crystallographic relationships in the mapped regions. It should be noted that these techniques record interactions volumes compared to essentially the surface information of low-kV BSE imaging. This interaction volume compromises some of the ultimate spatial resolution since the resulting EDS or EBSD signal comes from volume of 0.75 to 1.0 μm at best. Further these techniques are often an order of magnitude slower than BSE imaging due to the limitations of microanalytical detectors.

Segmentation is a classical image processing approach used for the consistent and non-subjective assignment of specific pixels to groupings within images. Advanced image processing algorithms, including segmentation, are widely used across many scientific

disciplines, for image analysis problems at all scales and complexities (Soille and Ansoult 1990; Rossouw et al. 2015). However, these algorithms are seldom employed in geological sciences (Barraud 2006; Wang 2007), despite accurate determination of grain size and textures being paramount to our understanding of geological processes.

Inaccuracies and inefficiencies of manual image segmentation for grain-size analysis are addressed here by, leveraging the open-source image processing Python libraries, hyperspy (de la Peña et al. 2019) and scikit-image (van der Walt et al. 2014) implemented with interactive Jupyter notebooks to deploy a *watershed segmentation workflow*. The watershed algorithm is used here to pull spinel grains out of the background and isolate individual grains. This method can be traced back to the 19th century (Maxwell 1870), through modifications in the 1980's (Beucher 1982) to their current form in many segmentation procedures (Najman et al. 2011).

This computer vision approach improves grain size estimation by 20% via automatic identification of individual and touching gains, prior to calculating their respective 2D grain metrics, including area and center of mass. The sensitivity of the algorithm to local contrast variations increases the overall number of particles measured, across the entire grain size distribution, compared with manual user approaches. The robust workflow has minimal research bias and processes entire data sets at a fraction of the time usually taken through manual techniques alone. We test and apply the workflow to new grain growth kinetic experiments on spinel-orthopyroxene aggregates relevant for xenolith exhumation rates. The system investigated as part of this study is chemically simple and therefore imaging from SEM methods was sufficient to produce many quality images for use with automated segmentation.

Methods

High pressure experiments

Grain growth experiments were performed on a 50:50 spinel-orthopyroxene mixture picked from a natural spinel peridotite from Lanzarote (Carracedo et al. 1992; Neumann et al. 1995; Bhanot et al. 2017) and ground under propanol to a starting grain size of around 0.1 μm. The use of a McCrone micronizing mill minimized crystal-structural damage, whilst ensuring a uniform fine grain size which was important in ensuring that steady-state grain growth was achieved rapidly during the annealing experiments. Experiments were annealed at pressures and temperatures appropriate for the spinel lherzolite stability field (1.2 – 1.65 GPa and 1323 - 1473 K) using a standard 18/11 multi-anvil cell assembly. Run durations ranged from 2 - 120 hours and were performed using the multi-anvil apparatus at University College London. All experimental conditions are reported in Table 1.

Analytical techniques

After temperature quench and overnight decompression, samples were recovered and set in epoxy resin before polishing to the center of each capsule. Samples were polished to a 3 μm diamond finish providing a satisfactory finish for imaging of spinel grains, further polishing was not possible as individual grains began to pull out leaving holes in the sample (observed as black grain shaped regions in each of the sample micrographs in Figure 1). Orthopyroxene grains appeared as large single crystals and poorly defined grain boundaries (Figure 1), orthopyroxene was also more susceptible to polishing scratches than spinel grains. The poorly defined grain boundaries and damaged surfaces of orthopyroxene were not clearly visible enough to analyze as part of this study. Fortuitously, due to the initial 50:50 ratio of spinel to orthopyroxene measuring just one phase is sufficient to determine grain growth kinetics of the two-phase system.

Appropriate imaging of the samples is crucial to the success of any form of image

segmentation. 2D imaging techniques (scanning electron microscopy) were chosen for time efficiency and a compromise between sample preparation and final image quality. EBSD as discussed earlier is another popular 2D imaging technique but inappropriate for the samples of this study, due to low throughput and preferential polishing of phases. Chemical colloidal polishing increases surface topography on multi-phase samples of varying hardness, resulting in poor mineral indexing.

Polished samples were imaged at UCL using the JEOL JSM – 6480LV scanning electron microscope (SEM). The SEM was operated in backscattered electron imaging mode (BSE) at 15 kV accelerating voltage and a beam current of approximately 10 nA. BSE imaging offers improved phase contrast compared with secondary electron imaging since the scattering strength is a positive function of the mean atomic number and density. Scattering intensity from surface roughness, scratches and local topography (such as polish height difference between Spinel and Orthopyroxene) are minimized with BSE compared to SE and EBSD. The high density and Fe- and Cr- enriched spinel grains have a high scattering intensity compared to the lower density matrix phase. In cases where the spatial resolution was not sufficient, additional higher-resolution imaging was conducted at Cardiff University using the Zeiss Sigma HD Field Emission Gun Analytical SEM at 15 kV accelerating voltage, 120 µm aperture and 4 nA beam current.

A total of eleven high pressure experiments were conducted, with three temperature-time series investigated throughout PT conditions appropriate to the spinel Lherzolite stability field. Following high pressure, high temperature experiments, seven to fifteen images per experiment were collected through SEM-BSE imaging. Images were taken at different locations throughout the sample, to ensure any grain size variations due to thermal gradients within the sample were accounted for. Example images are shown in Figure 1. A total of 22 images, (two per experiment) were analyzed by automated

192 segmentation, whilst 30 images, (two to four per experiment) were analyzed manually,
193 using the areas of equivalent circles technique.

194 Grain size estimation

195 Areas of equivalent circles

196 Grain size was manually measured from multiple BSE images from each experiment
197 (Figure 1) using the NIH - Image J software package (Schneider et al. 2012). Each easily
198 identifiable spinel grain in an image was manually drawn around, with clumped regions
199 dissected into several grains. Image J was then used to determine the areas of each grain,
200 which were subsequently converted to apparent radii. Results of manual grain size
201 analysis are reported in Table 1.

202 Orthopyroxene grains though present at approximately the same ratio as spinel were
203 not analyzed for grain size, due to poor visibility of grain boundaries and susceptibility to
204 polishing artefacts e.g. scratches and holes (Figure 1). Orthopyroxene grains could not be
205 easily identified by researchers and therefore attempting to resolve its grain size was not
206 undertaken as part of this study.

207 This procedure is prone to user bias; complex grain geometries can be difficult to
208 accurately draw around, segmentation of clustered grains can involve arbitrary choices
209 and small grains can be systematically underrepresented. In order to investigate the
210 reproducibility between researchers, the images were analyzed using this method by two
211 "expert" investigators who previously agreed criteria for definition of individual grains
212 and segmentation. It was found between the two expert users that, on average, there was
213 a 5 % difference in the average grain size measured on the same image, with a maximum
214 difference of 10 % in the measured grain size on the same image.

215 Standard error for all experiments ranged from 0.01-0.02 micrometers radius, for a
216 single expert investigator measuring grain size, except for E19-007, which has a much

larger standard error than all other experiments. The larger than expected standard error is attributed to the morphology of grains in this experiment, which are more interconnected than all the previous experiments (Figure 1 f), this makes determination of grain boundaries more difficult and therefore segmenting grains for measurement is highly uncertain. E19-007 was also separately imaged at UCL using a tungsten filament SEM, resulting in a poorer quality image than the other experiments which were imaged via FE-SEM at Cardiff University. Though grains are still highly visible against the background matrix, the poorly defined boundaries and greater clumping of grains resulted in a larger standard error. To ensure this standard error was representative and not due to misinterpretation by the investigator, over 800 grains were analyzed from four separate images each resulted with a large uncertainty on the average grain size.

This discrepancy is significantly larger than the standard error of the mean grain size for an experiment so, to further explore this, datasets were fitted to the grain growth law (Equation 2) using both the standard error from a single experimenter and a 5 % error as alternative weighting schemes.

Advanced image processing: watershed segmentation

A watershed segmentation workflow has been developed to allow implementation of user-independent reproducible measurements, which additionally increases the number of grains measured in each individual image. The workflow is flexible enough to allow analysis of multiple images from different experiments, which possess a range of grain sizes and mineral contrasts as imaged under varying brightness and contrast settings and across multiple instruments, all with minimum user intervention.

Our workflow is built in the open source language Python which provides access to advanced image processing and microscopy libraries such as Scikit- Image and Hyperspy (van der Walt et al. 2014; de la Peña et al. 2019). The workflow is implemented using

Jupyter Notebooks, providing an interactive method, not only for running the code, but documenting the process and user decisions (Kluyver et al. 2016). The workflow is available from GitHub details provided within supplementary materials. Our workflow, not only produces a segmented binary image, but through a process of particle labeling (built in function of Scikit-Image) can produce grain metrics for each individual object in the image. The workflow follows the structure shown in Figure 2.

Following imaging by SEM all micrographs were converted from RGB to 8-bit greyscale images, using the NIH-Image J software package (Schneider et al. 2012). This maintains the greyscale range of the micrographs but presents them to the workflow in a consistent data structure for analysis (Figure 2.1).

The entire watershed process seeks to accurately identify foreground objects (i.e. grains) from the background, whilst additionally pulling apart touching grains. This is accomplished through two iterations of the watershed process. The first defines the bright grain basins against the dark background, while the second iteration seeks to pull apart connected objects into individual grains.

Before initiating this process, the BSE greyscale intensity is normalized by assuming the inherent noise in the image is approximately Gaussian. Imaging filters can then be used quantitatively to denoise the greyscale intensity. For the BSE data in this report we employed filters which amplify contrast gradients, while preserving the texture of the image such as "total variation denoising" (TV) and "non-local means" (NLM) (Figure 2.2). The TV filter is more successful with poor quality noisy images which require amplification of the edge contrast e.g., sharpening in some areas whilst smoothing in the background (Chambolle 2004). NLM provides a higher quality result but requires an initial high quality dataset as, every pixel present is weighted based on the noise and normalized (Buades et al. 2005). We apply both filters to every BSE image, and

267 manually select which filter has best preserved the grains of interest from the original
268 image, whilst denoising the data. For the purposes of this study the NLM filter was used
269 for all experiments except E19-007, which was imaged at UCL. It was determined that
270 E19-007 was a lower quality image than those produced by FE-SEM imaging and
271 denoised most effectively by the TV filter.

272 An initial watershed iteration identifies spinel grains sitting in a background matrix.
273 We define grain basins by taking the derivative of the denoised image using a Scharr
274 filter, which identifies boundaries or edges between grains and the background matrix by
275 finding the greyscale gradient (Figure 2.3a). We compute and report the Otsu threshold, a
276 classical segmentation tool, used for splitting image data which is bimodal (Yousefi
277 2015). Its implementation does not capture all of the grains of interest, so we provide an
278 initial seed greyscale value, manually determined as 1.2 times the Otsu threshold. The
279 watershed algorithm then floods the grain basins of the Scharr image to define the
280 maximum extent of the bright foreground grains (Beucher 1994). This results in a binary
281 overlay image of lows (background = 0) and highs (grains = 1), which is used in
282 combination with the denoised greyscale image in subsequent processing steps.

283 Each of the foreground objects (preliminary interconnected grains) are labeled by
284 examining pixel connectivity. Preliminary metrics such as shape and size can be
285 calculated. At this stage the image still possesses pixels associated with bright specs and
286 holes which are artefacts of polishing. We remove the bright specs by manually cutting
287 out pixels corresponding to the highest 20 % greyscale intensity data from the processed
288 image. Holes are likewise addressed by applying morphological filters with Scikit-
289 Image, extreme values of the binarized image represent holes and are closed by
290 specifying the smallest number of pixels which represent the holes (van der Walt et al.
291 2014).

For the second watershed iteration (Figure 2.7) we cut apart interconnected grains in the binary image by calculating the distance between grain edges and the center of a grain basin. These distances define the secondary basins which are cut apart, by looking for saddles in the distance map. Further, to minimize over-segmentation (which is a known problem of watershed methods) we set a minimum distance to be considered (h-minima) (Malpica et al. 1997). Distances below this threshold, of 2 pixels, are considered to be part of a larger grain. This clearly marks where a boundary is required and the second watershed algorithm is used to segment on the saddled regions only, thus separating touching grains. Subsequent labeling of the individual grains allows for the automatic calculation of particle metrics. These metrics can then be inspected in the Jyputer notebook using Pandas data frames, or exported as a CSV file and explored using Excel (McKinney 2011). Reported metrics include the individual grain coordinates, grain area, eccentricity, minimum and maximum axis lengths.

Overlaying the labeled image onto the original BSE micrograph provides a qualitative method for the user to visually inspect the quality of the segmentation (Figures 2 and 3). A single image can be processed in under 3 minutes using the workflow presented here, a noticeable improvement in the efficiency of researchers compared to manual image processing which can take up to 15 minutes per image (Campbell et al. 2018).

Results

An example of manual grain identification is shown in Figure 3 e, incomplete grains, i.e. grains on the edges of BSE images, are ignored. The average grain size was determined from grain size distributions for each experiment as reported in Figure 4.

Representative images of the watershed workflow are displayed in Figure 3,

following image processing each segmented image required a visual check to ensure grains had been pulled apart appropriately in regions where clumping occurs, as well as removal of particle metrics associated with grains on the edges of images e.g., partially visible grains. In some images, very small particles were identified on the scale of a few (1-10) pixels, these tiny particles were also removed from the particle metrics list as they represent objects below the resolution of the SEM micrographs. Finally, clumped regions which had been unsuccessfully segmented were manually removed as they skew the apparent grain size to a larger average e.g., Figure 3, c. However, the under-segmented regions which were removed were not significant compared to the number of grains identified and their removal did not (2-7 %, reduction in total grains measured) change the determined average grain size, within error.

After visual inspection and conversion of particle area to equivalent radii, a 2D grain size distribution can be determined for each experiment and compared to those of hand-picked grains (Table 1). Figure 4 shows grain size distributions for manual and automated segmented analyses. Both manual and automated image processing procedures produce log-normal grain size distributions, with the average grain size being a positive function of temperature and time as expected (Hillert 1965; Atkinson 1988). Log-normal grain size distributions are expected for normal grain growth, when estimating grain size from 2D techniques, and provide a satisfactory solution describing grain growth in 3D space (Hillert 1965; Saetre 2002; Rios and Zöllner 2018). The resulting average grain size estimates from both methods is provided in Table 1.

The watershed algorithm is able to uniquely identify more grains than the manual approach for a given image, as shown in Figure 2. The grain size distribution plots (Figure 4) show that the tails of distributions from automated segmentation extend to smaller grain sizes than manually segmented distributions. Additionally, the grain size

distributions are more complete across the entire range of measured sizes, demonstrating not only are smaller grains missed from manual techniques but sampling across the entire distribution is more accurate with the watershed algorithm.

The largest differences in average grain size between the two techniques are seen in the longest duration experiments, suggesting smaller grains have not been identified by manual techniques (Figure 4. a and c). Although, the grain size distribution is expected to show an increased average number of large grains, the shape of these distributions should remain almost constant for the relatively small experimental durations investigated here. All experiments had a smaller average grain size when analyzed by automated techniques, except for E16-088 and E16-085 (Figure 4.b), which increased in grain size by 0.9 μm and 0.3 μm, respectively. These two experiments were in fact conducted at the same *PTt* conditions, 6 hours at 1373 K. It would be expected that their estimated average grain size would agree within error, and whilst this is the case for a consistent method of analysis (automated or manual), the grainsize increase by automated techniques may suggest over segmentation by the user when cutting interconnected grains.

Kinetic parameters for grain growth

While this study is not primarily about the kinetic grain growth mechanisms of spinel-orthopyroxene aggregates, calculated kinetic parameters can provide a valuable measure of the quality of the estimated "average grain size". In addition, they are used to constrain the grain growth mechanism and rate controlling species from many experimental grain growth studies, and to extrapolate experimental datasets to geological timescales (Karato 1989; Yamazaki et al. 1996, 2005, 2010; Faul and Scott 2006; Nishihara et al. 2006; Hiraga et al. 2010a).

A weighted non-linear least-squares fitting to the grain growth law expressed as $G = [kt + G_0^n]^{1/n}$, was performed for each of the manual and watershed grain size distributions. Grain size (G) was the dependent variable and an effective variance method was used as the weighting scheme for the non-linear least-squares fitting. This weighting scheme was chosen to reflect the uncertainty in both the dependent and independent variables (Orear 1982), resulting in a more accurate solution to unknown parameters, and error estimates closer to the true error which are commonly underestimated by minimizing the weighted sum of the squared deviation.

A second fitting was performed with the additional 5 % error on the mean grain size of manually analyzed grains, representing the inter-user error.

The grain growth exponent, *n*, is often expected to return a theoretical value of 2, where normal grain growth is occurring in a simple single phase system (Hillert 1965). Polyphase grain growth, is expected to yield values of 3, 4 or 5 for Zener-pinned grain growth, limited by diffusion through the lattice, along grain boundaries or along line defects ("pipe diffusion") respectively (Evans et al. 2001; Tsujino and Nishihara 2009).

The *n* values returned here range from 2.38±0.12 to 4.15±0.17, implying a range of coarsening processes may be operating. Aside from the grain growth exponent which may be indicative of the rate limiting process, activation enthalpy is often considered a good indicator of which species is rate limiting. The results from the regressions fall at values between 297±7.6 - 320±11 kJ mol^{-1}.

The resulting kinetic parameters for manual and automated segmentation are reported in Table 2.

Discussion

Textural recovery

Employing machine vision techniques, even in a supervised manner as demonstrated here, provides a methodology for identifying complex anhedral grains. Figure 5 demonstrates the watershed algorithm identifying clumped or touching grains while maintaining a visually realistic morphology. Our workflow saves time by rapid analysis (under 3 minutes per image), minimizes user bias and provides a consistent alternative to manual grain tracing methods.

The watershed workflow has been successful in identifying grains from complicated textures such as Figure 3 b. Many of the spinel grains exhibit bright chromium rich cores with small rims of more aluminum rich spinel; these tend to dominate the shorter duration experiments. The resulting texture is challenging to interpret as the contrast between the background orthopyroxene and rims of spinel is small. However, the subtle difference in greyscale, following the first watershed to remove the orthopyroxene background, is sufficient to allow grains to be segmented from one another (Figure 3, d).

Our segmentation workflow has been calibrated for a multiphase system and therefore takes advantage of bimodal greyscale intensities between the spinel and orthopyroxene grains. Grain analysis in a single-phase system would in principle allow for the skipping of the first watershed transform, since there is no background. This would be similar to the Ti-α grains segmented in Campbell et al., (2009). For any single-phase system to be successfully segmented there needs to be contrast between the grains. For some polycrystalline materials this may not be apparent in BSE imaging, like the orthopyroxene phase in our present experiments. To understand the grain structure of that phase other more time intensive microscopy techniques would need to be considered such as EBSD. This would allow for the mapping of grains based on variations in orientation. Ultimately, the EBSD grain orientation data comes from an orientation map

413 which needs to be segmented based on the misorientation angle, which like any
414 segmentation threshold is user defined. Alternately, this data can be segmented using a
415 watershed with threshold examining from the disorientation distribution.

416 For cases where EBSD is clearly the superior technique, it should be noted that this
417 comes at a cost of throughput or spatial resolution. Wright (2010) highlights that to
418 acquire maps of just 250 grains via EBSD can take anywhere between 1.8 and 7.5 hours,
419 dependent on the age of the instrument and resolution required. Higher throughput could
420 be achieved, but for the spatial resolution required in these studies, the smallest grains
421 would not be resolved. Additionally, beam interaction effects would need to be
422 considered (Wright 2010). It should also be noted that the samples in this study and in
423 many geological systems require uniform polishing for EBSD analysis which has proven
424 to be challenging. For the present samples, orthopyroxene preferentially polished with
425 respect to spinel leaving surface roughness which is unsuitable for EBSD analysis. For
426 high throughput analysis of multiphase systems where the absolute grain orientation is
427 not a concern but statistically meaningful grain size distributions are required BSE-SEM
428 imaging becomes a preferable cost-effective solution (Hillert 1965; Evans et al. 2001).
429 SEM imaging in combination with the segmentation workflow presented here, offers an
430 excellent alternative for rapid imaging and data analysis, which can all be achieved at a
431 fraction of the time.

432 Grain size distributions

433 The tails on grain size distributions from manual methods, (Figure 4) demonstrate user
434 bias to systematically picking larger grains and ignoring smaller ones. Subtle changes in
435 greyscale within SEM micrographs mask smaller grains which are difficult to uniquely
436 differentiate from the inherent noise within images. Providing a minimum pixel size for

437 the smallest truly "visible" grain within the resolution of SEM micrographs, reduces the
438 number of very small grains sampled in the automated segmentation approach, as can be
439 seen in the left-hand sides of Figure 4 a and c.

440 As well as identifying a greater number of small grains from images, automated
441 segmentation is also more representative of the “average” grain size. This is clearly
442 demonstrated by greater sampling of grains across the entire distribution, not just at
443 extreme small grain size values, as shown in Figure 4. Thus, the adjustment of average
444 grain size to smaller values is not exclusively related to increased sampling of small
445 grains; as there is an increase in grain identification and sampling across the whole
446 distribution. Further suggesting the average grain size from manual techniques is
447 misrepresentative of the distribution due to under sampling across the whole distribution.

448 The greatest discrepancies in average grain size were seen in experiments with the
449 largest grain sizes, corresponding to longer duration experiments and higher
450 temperatures. This may be due to the systematic over picking of large grains by the user,
451 during the image-analysis stage, using the areas of equivalent circles technique. This
452 shifting of the average grain size to large values has consequences for the interpretation
453 of grain growth kinetics, determined from these values.

454 The mean grain size was estimated from the grain size distributions and it was
455 found that both techniques returned a similarly small standard error on the mean grain
456 size for a measured population. Importantly, the discrepancy of the larger than
457 expected standard error for E19-007 from manual techniques, is now within the
458 range of values from automated techniques, implying better sampling and accurate
459 error determination from automated techniques. The difference in mean grain size
460 between the two independent expert investigators was found to be approximately 5% of
461 the mean grain size, some two to ten times greater than the formal error. This

462 discrepancy was found to be even larger when comparing results from inexperienced
463 (third-year undergraduate) investigators. Even with a small 5 % error between users, this
464 can lead to substantially different grain growth kinetics and thereby grain growth
465 mechanism, as will be shown below.

466 Grain growth kinetics

467 All the values of *n* obtained through the two methods of grain size analysis are
468 theoretically possible for a system of polyphase grain growth, suggesting grain growth in
469 this system is Zener-pinned and limited by diffusion along grain boundaries or through
470 the lattice. Values are also consistent with observations from grain growth studies in
471 other upper mantle phases, for example Hiraga et al., (2010) who conducted grain growth
472 experiments on forsterite-enstatite aggregates and found *n* values ranging between 3 and
473 5, for a consistent method of grain size analysis and varying proportions of their
474 secondary phase, enstatite. Our *n* values fall within a similar range, suggesting these are
475 typical values of upper mantle phases (Figure 6). However, we find a very large
476 difference in *n* between the manual and automated methods (2.38 and 4.15
477 respectively). This difference would be interpreted as different mechanisms, either
478 interface diffusion or grain boundary diffusion (Evans et al. 2001; Kim et al. 2004).
479 Either case has a different grain growth exponent and could imply a variety of diffusive
480 mechanisms may be responsible for the rate limiting step.

481 This disparity between kinetic solutions for the two analysis methods is however
482 reduced, when the formal error on the average grain size is modified to 5 % of the mean
483 grain size (Table 2). Most influential to the determined kinetic parameters is the
484 treatment of E19-007, as the grain growth exponent is effectively pinned by the longest
485 duration experiment. Manual techniques consistently underestimate the standard error,
486 whilst automated approaches result in larger and perhaps more realistic formal errors. By

accommodating the true errors on manual measurement approaches, the grain growth exponent is more consistent to higher values of n, (3.47±0.23 to 4.15 ±0.17). Yet these values still imply very different dominant diffusive mechanisms and an averaged grain growth exponent for the system based on both techniques, would be subject to large uncertainties and makes determining the grain growth mechanism troublesome.

But more importantly, large uncertainties in n also reduces the possibility of accurately extrapolating grain size through time. The small variations in the grain growth exponent here, lead to differences of greater than 25 % in the predicted grain size at only 14 days (Figure 6). This difference is even more pronounced when assuming the initial errors on the mean grain size from manual approaches are accurate. The divergence of predicted grain size increases with time, and eventually the confidence intervals overlap across widely different temperatures (Supplementary Figure 1). The problem of large uncertainties in the grain growth exponent is often dealt with by fixing n for the purposes of extrapolation (Yamazaki et al. 2005; Nishihara et al. 2008; Hiraga et al. 2010a). However, as shown here even small uncertainties in n significantly alter extrapolated grain sizes through time, as well as potentially changing interpretation of the grain growth mechanism. Thus, fixing n, to possibly the wrong value, will produce misleading predictions. Making interpretations on the grain growth mechanism and extrapolated grain size subject to large unconstrained uncertainties.

Despite the challenges in evaluating grain size through time, the activation enthalpy from the manual + 5 % error approach, almost agrees within error of the automated solution at 278±19 - 320±11 kJ mol^{-1}, respectively. This suggests Fe-Mg diffusion in orthopyroxene may be the rate limiting step in coarsening of this two phase spinel-orthopyroxene system (Dohmen et al. 2016). The prediction of the same rate limiting species, by both methods of analysis, suggests a significant amount of time has

512 passed and the rate limiting species now has an influence on coarsening of the system.
513 Dohmen et al., (2016) measured the interdiffusion coefficients of Fe-Mg in
514 orthopyroxene, which takes place through lattice diffusive mechanisms, whilst the
515 activation enthalpy now agrees within error of their estimates (308±23kJ mol^{-1}), a grain
516 growth exponent of 3 would be expected in the case of lattice diffusion. Both methods of
517 analysis return grain growth exponents greater than 3, demonstrating the challenge in
518 accurately determining both the rate limiting mechanism and species.

519 Although the kinetic solutions presented here are subject to large uncertainties,
520 automated segmentation still presents the most satisfactory interpretation of spinel grain
521 growth. We do not report further predictions on grain size through geological time for the
522 reasons discussed above. Further investigations are required to determine the accuracy of
523 grain size and its eventual use to constrain grain growth kinetics, caution is emphasized
524 when using small experimental data sets to constrain such kinetic parameters as has been
525 commonplace for many grain growth studies (Hiraga et al., 2010; Nishihara et al., 2004;
526 Tsujino and Nishihara, 2010; Yamazaki et al., 2010, 2005, 1996).

527 Large uncertainties, such as the ones reported here, are common within grain growth
528 studies focused solely on image analysis (Yamazaki et al. 1996, 2005, 2009; Nishihara et
529 al. 2006; Hiraga et al. 2010a). This demonstrates the need to go beyond only collecting
530 SEM-BSE data. Combining grain size measurements with analytical techniques like
531 energy dispersive spectroscopy, electron back-scattered diffraction or high resolution 3D
532 X-ray micro tomography would unlock important information about the mechanisms for
533 grain growth. Using correlative and machine learning approaches, all these datasets can
534 be combined to form quantitative statistical descriptions of the grain growth kinetics
535 (Einsle et al. 2018).

Implications

The automated watershed workflow presented here appears to improve the reproducibility of grain size measurements while increasing the yield of grains measured compared to traditional manual approaches. This workflow demonstrates a clear advantage in the minimization of user bias, but many of the parameters required manual tuning to produce an optimal "realistic" measurement. Additionally, the speed at which datasets can be analyzed is greatly enhanced with the use of automated techniques.

One of the biggest areas of active research relates to the use of machine learning and artificial intelligence to improve the segmentation of images. These data driven approaches offer further advantages in that the segmentation criteria become defined by examining the statistics of an image set and looking at variations of different image filters applied to the same image. This works particularly well when examining tomographic data sets generated by micro CT or FIB-SEM tomography techniques. Great progress has recently been made applying clustering or neural network techniques to these large data sets (Andrew 2018). Clustering analysis may offer the best path forward for small data sets like the ones presented here. Tomographic imaging, by contrast, produces data sets with hundreds to thousands of images, offering the most advantage for supervised machine learning tools. With the rise in automated mapping techniques, it should be possible to collect large numbers of BSE images across an entire thin section, or collections of sections. Batch processing would benefit from supervised machine learning enabled workflows.

The rapid collection of large volumes of data would result in better estimates of grain size and therein grain growth kinetics. To this end, and to further the implementation of automated segmentation and facilitate improvements in grain size estimation, there needs

560 to a community move towards greater data sharing and accesses as has been advocated
561 for within the geological sciences community (Stall et al. 2019).

562 We have highlighted systematic biases in interpreting grain size from 2D images
563 including; the exclusion or misinterpretation of small grains by traditional analysis
564 techniques alongside grain size distributions misrepresentative of the mean grain size.

565 The automated workflow described here can therefore significantly improve grain size
566 distributions by accounting for missing data, across the entire distribution. We
567 acknowledge the challenges in extrapolating grain size to geological time and present a
568 first attempt to address this problem by improving grain size analysis. Additionally we
569 present a kinetic solution to the grain growth of spinel-orthopyroxene aggregates, which
570 represents coarsening of a two phase system, limited by Mg lattice diffusion in
571 orthopyroxene (Dohmen et al. 2016). To address the uncertainties in experimentally
572 determined grain growth exponents, much longer duration annealing experiments are
573 required, beyond those usually possible in high pressure, high temperature apparatus. It
574 is for this reason that the data, which is available, must be treated in a systematic,
575 reproducible manner. As demonstrated here, small changes in only the reported 1 ε-
576 errors can lead to misinterpretations of the grain growth kinetics. However further
577 improvements are needed in the determination of experimental grain sizes before kinetic
578 solutions can be applied to the Earth.

579 We have demonstrated our segmentation workflow is able to rapidly process multiple
580 SEM images in a consistent and repeatable manner, from an initial complex grayscale
581 image. Automated segmentation vastly increases the number of grains identified and
582 indexed per 2D image, as compared to expert researchers analyzing the same images (see
583 Table 1). The number of grains identified and indexed by automated segmentation shows

584 an impressive 68 % increase as compared to manual techniques alone (7264 grains
585 compared to 4314). This alone, demonstrates the power of utilizing computer vision for
586 grain analysis and also results in a coherent kinetic solution.

587 Acknowledgements

588 We thank James Davy for assistance with SEM imaging at UCL and Duncan Muir for
589 imaging at Cardiff University. The 'inexpert investigators' were third-year
590 undergraduate students at UCL (GEOL0039; 2018-19 cohort). We thank two anonymous
591 reviewers for their comments, which helped improve this manuscript and Bin Chen for
592 their editorial handling. This work was part of ISE's NERC-funded Ph.D (award
593 NE/M00046X/1 to JB and DD). JFE acknowledges funding under ERC Advanced Grant
594 320750-Nanopaleomagnetism.

This is the peer-reviewed, final accepted version for American Mineralogist, published by the Mineralogical Society of America.
The published version is subject to change. Cite as Authors (Year) Title. American Mineralogist, in press.
DOI: https://doi.org/10.2138/am-2021-7797. http://www.minsocam.org/

				Manual		Watershed	
Experimental run	P (GPa)	T (K)	Time (h)	Average grain size (μm)	No. identified	Average grain size (μm)	No. identified
E17 - 050	1.2	1323	6	0.46 (0.01)	325	0.41 (0.01)	603
E17 - 053	1.2	1323	25	0.63 (0.01)	239	0.47 (0.01)	525
E17 - 059	1.2	1323	48	0.65 (0.01)	299	0.50 (0.01)	678
E17 - 016	1.2	1373	2	0.39 (0.01)	353	0.37 (0.02)	686
E16 - 088	1.4	1373	6	0.50 (0.02)	450	0.59 (0.01)	647
E16 - 085	1.2	1373	6	0.47 (0.02)	503	0.50 (0.09)	578
E18 - 003	1.4	1373	24	0.74 (0.02)	250	0.64 (0.01)	286
E17 - 017	1.65	1473	3	0.63 (0.02)	323	0.51 (0.01)	434
E17 - 018	1.65	1473	6	0.78 (0.02)	219	0.61 (0.03)	749
E16 - 090	1.65	1473	18	1.30 (0.01)	492	0.89 (0.01)	975
E19 - 007	1.65	1473	120	1.74 (0.20)	861	1.30 (0.03)	1103

Table 1: Experimental run conditions and results from area of equivalent circles method, Python automated segmentation workflow. All grain sizes are reported as radii, values in parenthesis are one standard error on the mean grain size.

597

598

Measurement Method	Log k_0	ΔH ($kJmol^{-1}$)	n	G_0(μm)
Manual	$10^{5.61\pm5.43}$	287±7.6	2.38±0.12	0.37±0.01
Manual + 5% error	$10^{5.15\pm5.37}$	278±19	3.47±0.23	0.30±0.05
Watershed	$10^{6.27\pm6.23}$	320±11	4.15±0.17	0.38±0.01

599

600 Table 2: Kinetic grain growth parameters returned from non-linear least- squares
601 fitting, to all experimental data.

602

603

This is the peer-reviewed, final accepted version for American Mineralogist, published by the Mineralogical Society of America.
The published version is subject to change. Cite as Authors (Year) Title. American Mineralogist, in press.
DOI: https://doi.org/10.2138/am-2021-7797. http://www.minsocam.org/

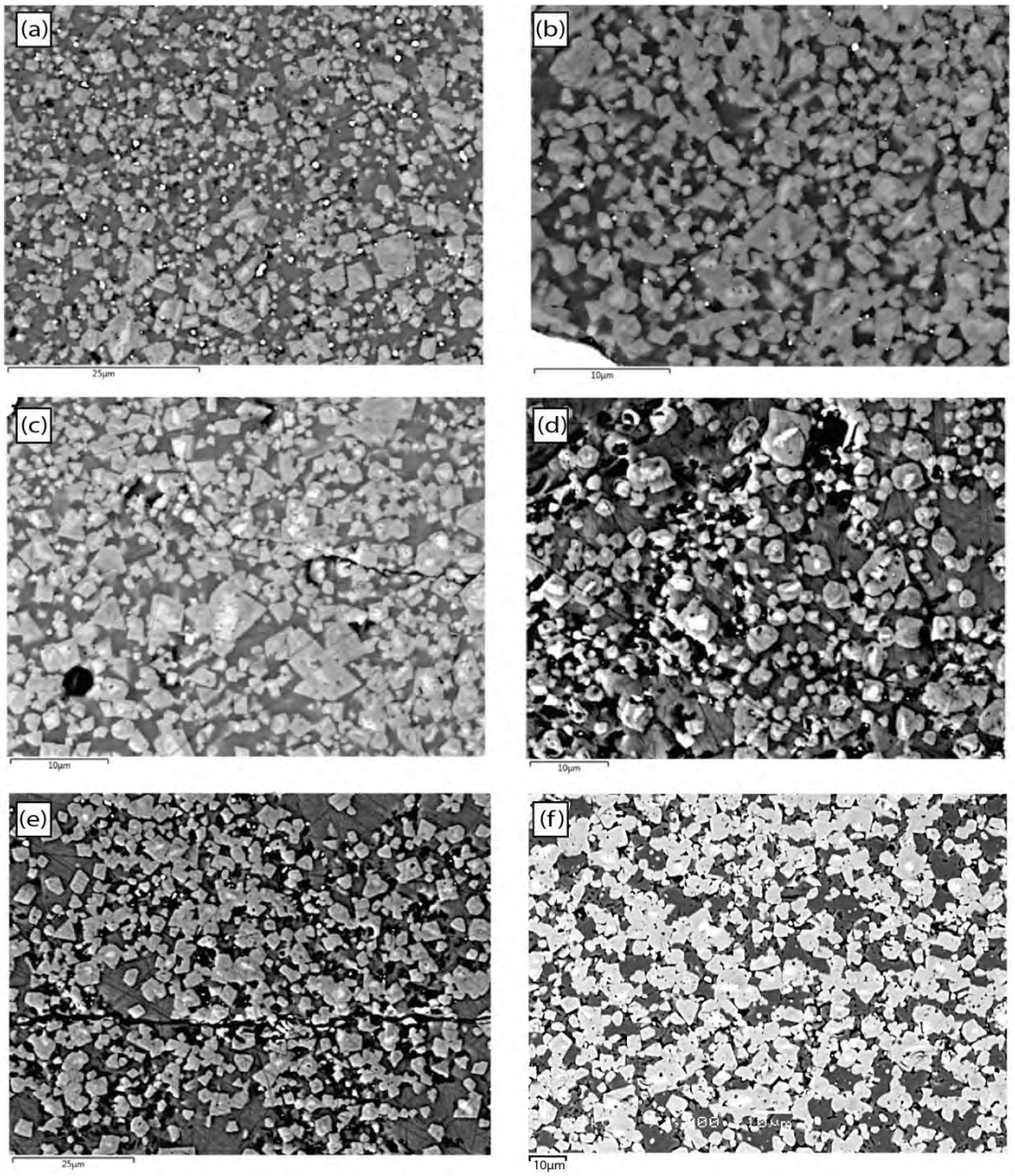

Figure 1: BSE micrographs of recovered high PT experiments, (a) E17-050 (1323 K, 6 hours). (b) E17-053 (1323 K, 25 hours) (c) E17-016 (1373 K, 2 hours) (d) E17-018 (1473 K, 6 hours) (e) E16-090 (1323 K, 18 hours) (f) E19-007 (1373 K, 120 hours). Micrographs are ordered in increasing experimental temperature and duration. For complete run conditions see Table 1. Spinel grains are clearly visible as euhedral to subhedral grains with bright chromium cores. The matrix material is orthopyroxene +/- clinopyroxene, dependent on the initial composition of the starting material.

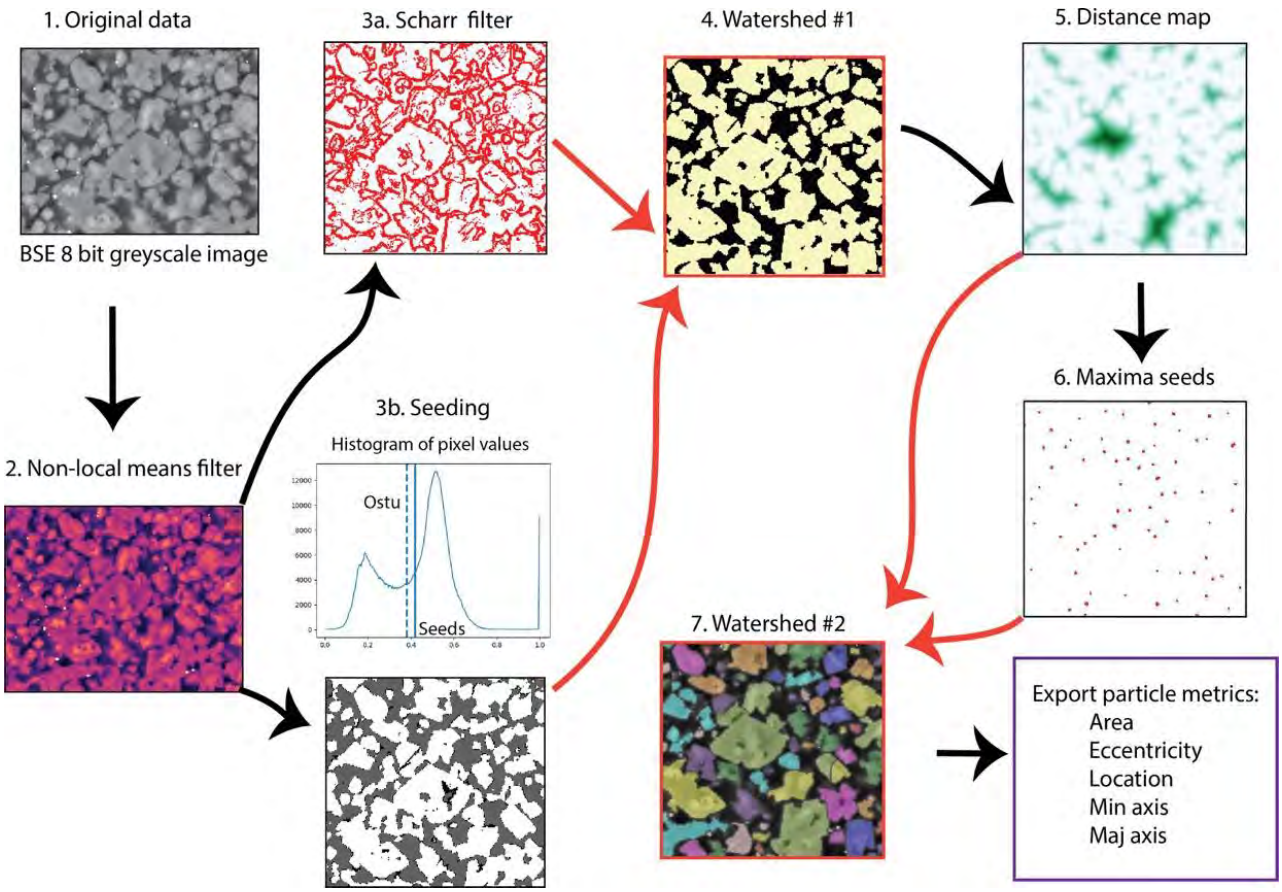

Figure 2: A simplified diagrammatic workflow of the image processing code developed for the analysis of spinel grain growth experiments. Images are first loaded in an 8-bit greyscale format and image processing filters are used to denoise the original image. In step 3, a Scharr filter is applied to identify grains. Step 4 pulls these away from the background matrix with the use of watershed A. At the same time an additional step is added to remove bright specks and fill in any holes present within the image. Step 5, interconnected grains are identified by peaks and basins in the greyscale intensity and shown as a distance map. Grain locations are highlighted by seeds and their positions represent the peaks in

627 greyscale intensity, i.e. this corresponds to the center of grains. In combination
628 with the distance map at step 7 watershed B is implemented to pull apart
629 interconnected grains from one another and the final result is overlain onto the
630 original BSE image for a visual end result. The addition of color in step 7 is
631 arbitrary and used to overlay segmented grains onto the original BSE image for
632 visual inspection.
633
634
635
636
637
638
639
640
641
642
643

This is the peer-reviewed, final accepted version for American Mineralogist, published by the Mineralogical Society of America.
The published version is subject to change. Cite as Authors (Year) Title. American Mineralogist, in press.
DOI: https://doi.org/10.2138/am-2021-7797. http://www.minsocam.org/

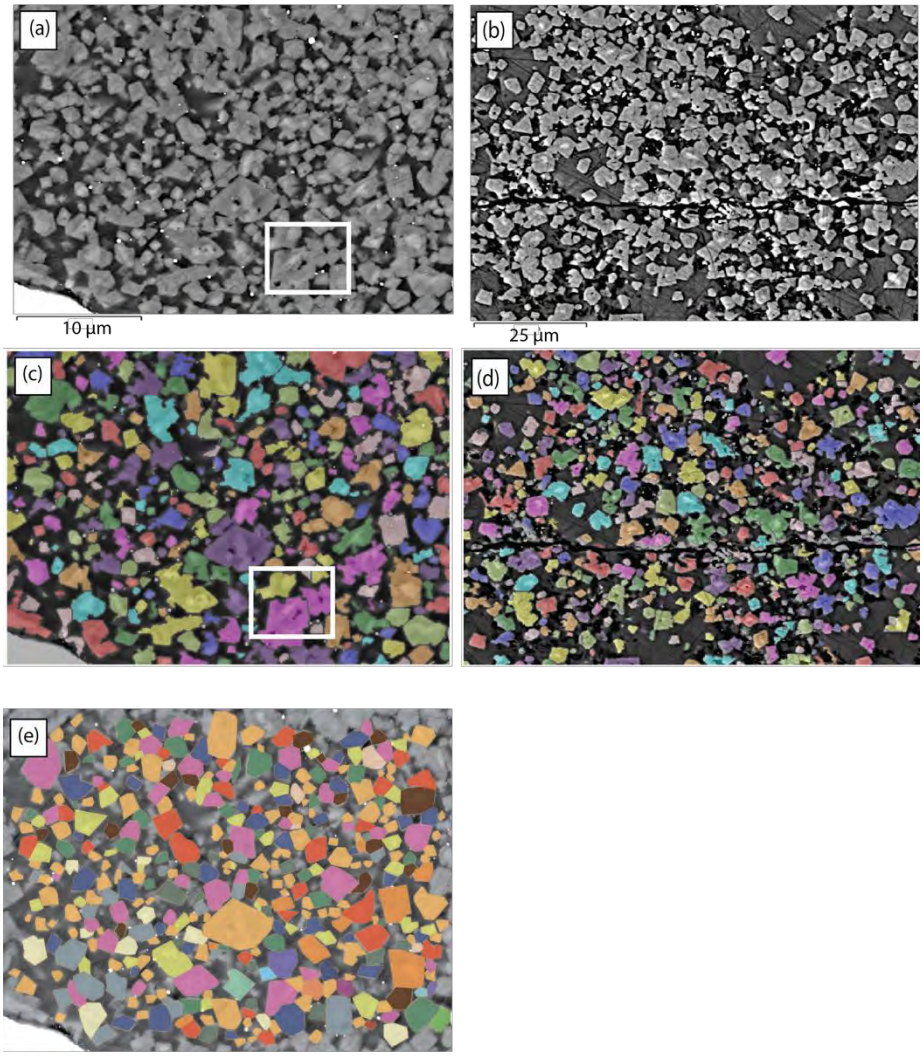

Figure 3: BSE micrographs from experiments (a) E17-053 and (b) E16-090. with their associated segmented images produced from the Python workflow below (c, d). The colored regions in c and d represent singular grains identified by the code. The majority of images are segmented, visually, well but regions of under-segmentation exist. The white highlighted region in c shows multiple grains which have been clumped together and interpreted as a single grain. (e) is an example of visually identified and hand-drawn grains using the NIH image - J software package.

This is the peer-reviewed, final accepted version for American Mineralogist, published by the Mineralogical Society of America.
The published version is subject to change. Cite as Authors (Year) Title. American Mineralogist, in press.
DOI: https://doi.org/10.2138/am-2021-7797. http://www.minsocam.org/

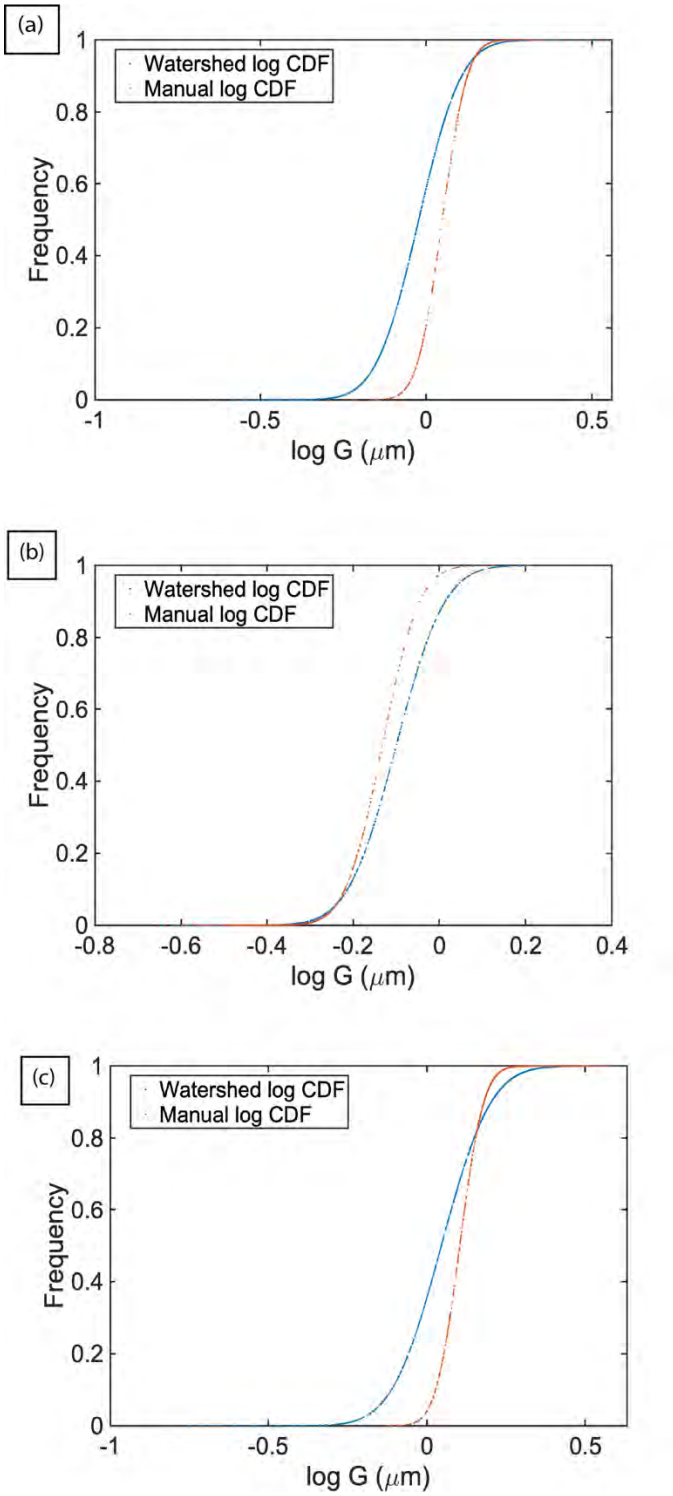

Figure 4: Log-normal distributions for user-analyzed grain sizes in orange and automated image segmentation in blue. (a) E16-090, (b) E16-088 and (c) E19-007.

662

663

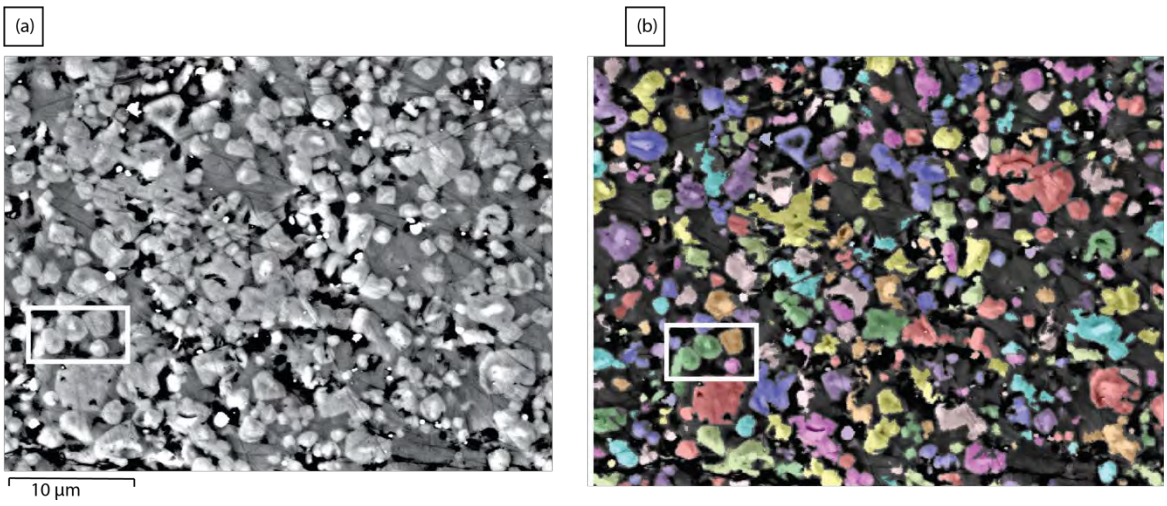

664

665 Figure 5: (a) SEM micrograph of E17-018 with its' segmented image in (b).
666 Regions highlighted in white boxes demonstrate the ability of automated image
667 segmentation to pull apart clumped grains whilst retaining their morphology.

This is the peer-reviewed, final accepted version for American Mineralogist, published by the Mineralogical Society of America.
The published version is subject to change. Cite as Authors (Year) Title. American Mineralogist, in press.
DOI: https://doi.org/10.2138/am-2021-7797. http://www.minsocam.org/

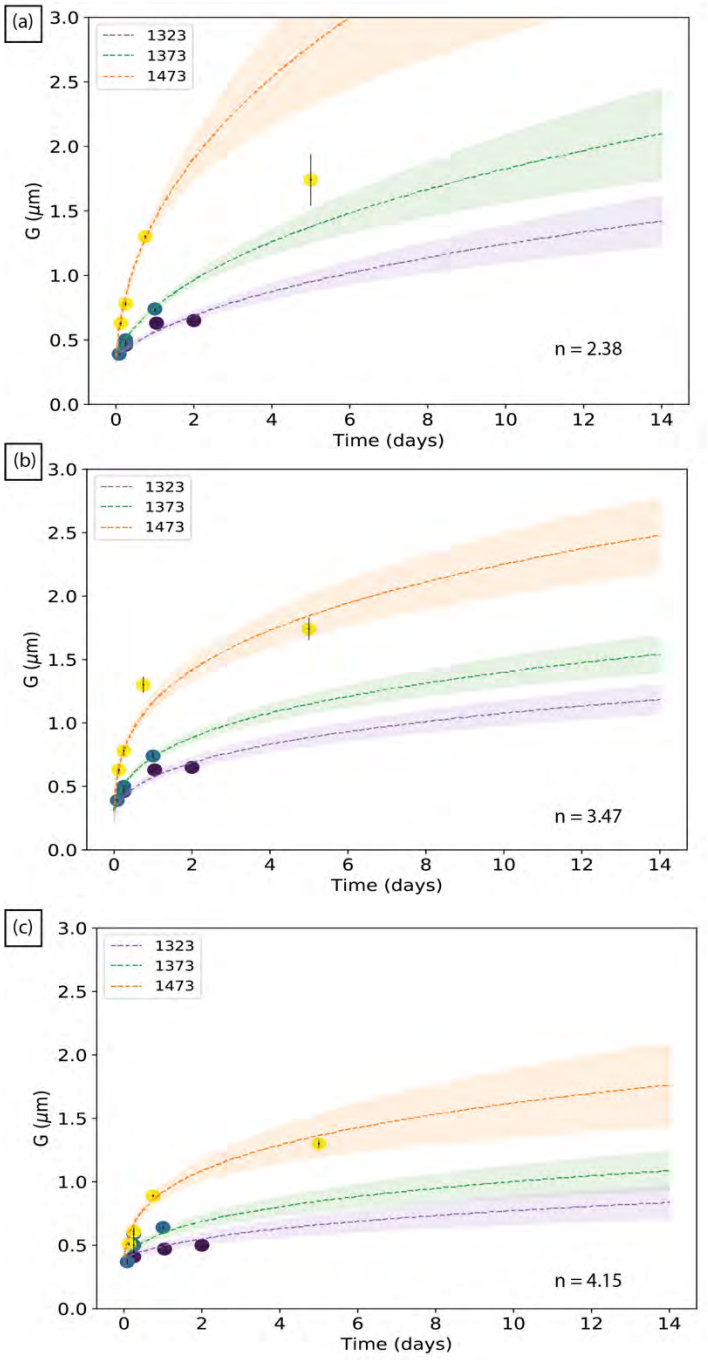

Figure 6: A global fit of grain size to the normal grain growth law, with expected 95 % confidence intervals for a period of 14 days. (a) Best fit solution from manual segmentation. (b) A fit to the grain growth law following image analysis from manual segmentation and an additional 5 % error, amongst multiple users. (c) The best fit solution for grain size estimated from automated watershed segmentation. *n* is the best fitting grain growth exponent for each data set.

675 # References

676 Abrams, H. (1971) Grain Size Measurements by the Intercept Method. Metallography, Vol.
677 4, 59-78.

678 Andrew, M. (2018) A quantified study of segmentation techniques on synthetic geological
679 XRM and FIB-SEM images. Computational Geosciences, 22, 1503–1512.

680 ASTM E112-13 (2012) Standard Test Method for Determin ing Average Grain Size. ASTM
681 International.

682 Atkinson, H. V. (1988) Overview no. 65. Theories of normal grain growth in pure single
683 phase systems. Acta Metallurgica, 36, 469–491.

684 Barraud, J. (2006) The use of watershed segmentation and GIS software for textural analysis
685 of thin sections. Journal of Volcanology and Geothermal Research, 154, 17–33.

686 Bercovici, D., and Ricard, Y. (2013) Generation of plate tectonics with two-phase grain-
687 damage and pinning: Source-sink model and toroidal flow. Earth and Planetary Science
688 Letters, 365, 275–288.

689 Beucher, S. (1982) Watersheds of functions and picture segmentation. ICASSP, IEEE
690 International Conference on Acoustics, Speech and Signal Processing - Proceedings,
691 1982-May, 1928–1931.

692 ——— (1994) Watershed, Hierarchical Segmentation and Waterfall Algorithm pp. 69–76.

693 Bhanot, K.K., Downes, H., Petrone, C.M., and Humphreys-Williams, E. (2017) Textures in
694 spinel peridotite mantle xenoliths using micro-CT scanning: Examples from Canary
695 Islands and France. Lithos, 276, 90–102.

696 Buades, A., Coll, B., and Morel, J.M. (2005) A non-local algorithm for image denoising.

Proceedings - 2005 IEEE Computer Society Conference on Computer Vision and Pattern Recognition, CVPR 2005, II, 60–65.

Burke, J.E., and Turnbull, D. (1952) Recrystallization and grain growth. Progress in Metal Physics, 3, 220–292.

Campbell, A., Murray, P., Yakushina, E., Marshall, S., and Ion, W. (2018) New methods for automatic quantification of microstructural features using digital image processing. Materials and Design, 141, 395–406.

Campbell, A.J., Danielson, L., Righter, K., Seagle, C.T., Wang, Y., and Prakapenka, V.B. (2009) High pressure effects on the iron-iron oxide and nickel-nickel oxide oxygen fugacity buffers. Earth and Planetary Science Letters, 286, 556–564.

Carracedo, J.C., Rodriguez Badiola, E., and Soler, V. (1992) The 1730-1736 eruption of Lanzarote, Canary Islands: a long, high-magnitude basaltic fissure eruption. Journal of Volcanology and Geothermal Research, 53, 239–250.

Chambolle, A. (2004) An Algorithm for Total Variation Minimization and Applications. Journal of Mathematical Imaging and Vision, 20, 89–97.

Chu, X., and Korenaga, J. (2012) Olivine rheology, shear stress, and grain growth in the lithospheric mantle: Geological constraints from the Kaapvaal craton. Earth and Planetary Science Letters, 333–334, 52–62.

Dannberg, J., Eilon, Z., Faul, U., Gassmöller, R., Moulik, P., and Myhill, R. (2017) The importance of grain size to mantle dynamics and seismological observations. Geochemistry, Geophysics, Geosystems, 18, 3034–3061.

de la Peña, F., Prestat, E., Fauske, V.T., Burdet, P., Jokubauskas, P., Nord, M., Ostasevicius, T., MacArthur, K.E., Sarahan, M., Johnstone, D.N., and others (2019, September 6)

720 hyperspy/hyperspy: HyperSpy v1.5.2.

721 Dobson, D.P., and Mariani, E. (2014) The kinetics of the reaction of majorite plus
722 ferropericlase to ringwoodite: Implications for mantle upwellings crossing the 660 km
723 discontinuity. Earth and Planetary Science Letters, 408, 110–118.

724 Dohmen, R., Ter Heege, J.H., Becker, H.W., and Chakrabortrty, S. (2016) Fe-Mg
725 interdiffusion in orthopyroxene. American Mineralogist, 101, 2210–2221.

726 Einsle, J.F., Martineau, B., Buisman, I., Vukmanovic, Z., Johnstone, D., Eggeman, A.,
727 Midgley, P.A., and Harrison, R.J. (2018) All Mixed Up: Using Machine Learning to
728 Address Heterogeneity in (Natural) Materials. Microscopy and Microanalysis, 24, 562–
729 563.

730 Evans, B., Renner, J., and Hirth, G. (2001) A few remarks on the kinetics of static grain
731 growth in rocks. International Journal of Earth Sciences, 90, 88–103.

732 Faul, U., and Jackson, I. (2005) The seismological signature of temperature and grain size
733 variations in the upper mantle. Earth and Planetary Science Letters, 234, 119–134.

734 Faul, U.H., and Scott, D. (2006) Grain growth in partially molten olivine aggregates.
735 Contributions to Mineralogy and Petrology, 151, 101–111.

736 Hillert, M. (1965) On the theory of normal and abnormal grain growth. Acta Metallurgica,
737 13, 227–238.

738 Hiraga, T., Tachibana, C., Ohashi, N., and Sano, S. (2010a) Grain growth systematics for
739 fosterite + enstatite aggreates: Effect of lithology of grain size in the upper mantle. Earth
740 and Planetary Science Letters, 291, 10–20.

741 Hiraga, T., Miyazaki, T., Tasaka, M., and Yoshida, H. (2010b) Mantle superplasticity and its

742 self-made demise. Nature, 468, 1091–1094.

743 Hirth, G., and Kohlstedt, D.L. (1995) Experimental constraints on the dynamics of the
744 partially molten upper mantle: 2. Deformation in the dislocation creep regime. Journal
745 of Geophysical Research: Solid Earth, 100, 15441–15449.

746 Karato, S. (1989) Grain growth kinetics in olivine aggregates. Tectonophysics, 168, 255–273.

747 Karato, S.I. (1984) Grain-size distribution and rheology of the upper mantle. Tectonophysics,
748 104, 155–176.

749 Kim, B.N., Hiraga, K., and Morita, K. (2004) Kinetics of normal grain growth depending on
750 the size distribution of small grains. Nippon Kinzoku Gakkaishi/Journal of the Japan
751 Institute of Metals, 68, 913–918.

752 Kluyver, T., Ragan-kelley, B., Pérez, F., Granger, B., Bussonnier, M., Frederic, J., Kelley,
753 K., Hamrick, J., Grout, J., Corlay, S., and others (2016) Jupyter Notebooks—a
754 publishing format for reproducible computational workflows. Positioning and Power in
755 Academic Publishing: Players, Agents and Agendas, 87–90.

756 Malpica, N., De Solórzano, C.O., Vaquero, J.J., Santos, A., Vallcorba, I., García-Sagredo,
757 J.M., and Del Pozo, F. (1997) Applying watershed algorithms to the segmentation of
758 clustered nuclei. Cytometry, 28, 289–297.

759 Maxwell, J.C. (1870) On hills and dales. The London, Edinburgh, and Dublin Philosophical
760 Magazine and Journal of Science, 40, 421–427.

761 McKinney, W. (2011) pandas: a Foundational Python Library for Data Analysis and
762 Statistics. Conference Proceedings.

763 Mendelson, M.I. (1969) Average Grain Size in Polycrystalline Ceramics. Journal of the

764 American Ceramic Society, 52, 443–446.

765 Najman, L., Couprie, M., Bertrand, G., Najman, L., Couprie, M., and Watersheds, G.B.
766 (2011) Watersheds , mosaics and the emergence paradigm To cite this version : HAL
767 Id : hal-00622113. Discrete Applied Mathematics, 147, 301–324.

768 Neumann, E.R., Wulff-Pedersen, E., Johnsen, K., Andersen, T., and Krogh, E. (1995)
769 Petrogenesis of spinel harzburgite and dunite suite xenoliths from Lanzarote, eastern
770 Canary Islands: Implications for the upper mantle. Lithos, 35, 83–107.

771 Nishihara, Y., Takahashi, E., Matsukage, K.N., Iguchi, T., Nakayama, K., and Funakoshi, K.
772 (2004) Thermal equation of state of (Mg0.91Fe0.09)2SiO4 ringwoodite. Physics of the
773 Earth and Planetary Interiors, 143–144, 33–46.

774 Nishihara, Y., Shinmei, T., and Karato, S.I. (2006) Grain-growth kinetics in wadsleyite:
775 Effects of chemical environment. Physics of the Earth and Planetary Interiors, 154, 30–
776 43.

777 Nishihara, Y., Tinker, D., Kawazoe, T., Xu, Y., Jing, Z., Matsukage, K.N., and Karato, S.
778 ichiro (2008) Plastic deformation of wadsleyite and olivine at high-pressure and high-
779 temperature using a rotational Drickamer apparatus (RDA). Physics of the Earth and
780 Planetary Interiors, 170, 156–169.

781 Orear, J. (1982) Least squares when both variables have uncertainties. American Journal of
782 Physics, 50, 912–916.

783 Rios, P.R., and Zöllner, D. (2018) Grain growth–unresolved issues. Materials Science and
784 Technology (United Kingdom), 34, 629–638.

785 Rossouw, D., Burdet, P., De La Peña, F., Ducati, C., Knappett, B.R., Wheatley, A.E.H., and
786 Midgley, P.A. (2015) Multicomponent Signal Unmixing from Nanoheterostructures:

Overcoming the Traditional Challenges of Nanoscale X-ray Analysis via Machine Learning. Nano Letters, 15, 2716–2720.

Saetre, T.O. (2002) On the theory of normal grain growth in two dimensions. Acta Materialia, 50, 1539–1546.

Schneider, C.A., Rasband, W.S., and Eliceiri, K.W. (2012) NIH Image to ImageJ: 25 years of image analysis. Nature Methods, 9, 671–675.

Soille, P., and Ansoult, M. (1990) Automated basin delineation from {DEM}s using mathematical morphology. Signal Processing, 20, 171–182.

Solomatov, V.S., and Reese, C.C. (2008) Grain size variations in the Earth's mantle and the evolution of primordial chemical heterogeneities. Journal of Geophysical Research, 113, B07408.

Solomatov, V.S., El-Khozondar, R., and Tikare, V. (2002) Grain size in the lower mantle: Constraints from numerical modeling of grain growth in two-phase systems. Physics of the Earth and Planetary Interiors, 129, 265–282.

Stall, S., Yarmey, L., Cutcher-Gershenfeld, J., Hanson, B., Lehnert, K., Nosek, B., Parsons, M., Robinson, E., and Wyborn, L. (2019) Make scientific data FAIR. Nature, 570, 27–29.

Tsujino, N., and Nishihara, Y. (2009) Grain-growth kinetics of ferropericlase at high-pressure. Physics of the Earth and Planetary Interiors, 174, 145–152.

——— (2010) Effect of pressure on grain-growth kinetics of ferropericlase to lower mantle conditions. Geophysical Research Letters, 37, 1–5.

van der Walt, S., Schönberger, J.L., Nunez-Iglesias, J., Boulogne, F., Warner, J.D., Yager,

N., Gouillart, E., Yu, T., and the scikit-image contributors (2014) scikit-image: image processing in Python. PeerJ, 2, e453.

Wang, W. (2007) Image analysis of size and shape of mineral particles. Proceedings - Fourth International Conference on Fuzzy Systems and Knowledge Discovery, FSKD 2007, 4, 41–44.

Wright, S.I. (2010) A Parametric Study of Electron Backscatter Diffraction based Grain Size Measurements. Practical Metallography, 47, 16–33.

Yamazaki, D., Kato, T., Ohtani, E., and Toriumi, M. (1996) Grain Growth Rates of MgSiO3 Perovskite and Periclase Under Lower Mantle Conditions. Science, 274, 2052–2054.

Yamazaki, D., Inoue, T., Okamoto, M., and Irifune, T. (2005) Grain growth kinetics of ringwoodite and its implication for rheology of the subducting slab. Earth and Planetary Science Letters, 236, 871–881.

Yamazaki, D., Yoshino, T., Matsuzaki, T., Katsura, T., and Yoneda, A. (2009) Texture of (Mg,Fe)SiO3 perovskite and ferro-periclase aggregate: Implications for rheology of the lower mantle. Physics of the Earth and Planetary Interiors, 174, 138–144.

Yamazaki, D., Matsuzaki, T., Yoshino, T., Suetsugu, D., Bina, C., Inoue, T., Wiens, D., and Jellinek, M. (2010) Grain growth kinetics of majorite and stishovite in MORB. Physics of the Earth and Planetary Interiors, 183, 183–189.

Yousefi, J. (2015) Image Binarization using Otsu Thresholding Algorithm. Research Gate.